

1 **Characterization of aerosol hygroscopicity, mixing state, and**
2 **CCN activity at a suburban site in the central North China Plain**

3

4 **Yuying Wang¹, Zhanqing Li¹, Yingjie Zhang², Wei Du^{2,3}, Fang Zhang¹, Haobo Tan⁴,**
5 **Hanbing Xu⁵, Tianyi Fan¹, Xiaoai Jin¹, Xinxin Fan¹, Zipeng Dong¹, Qiuyan Wang⁶, Yele**
6 **Sun^{2,3}**

7

8

9 ¹College of Global Change and Earth System Science, Beijing Normal University, Beijing 100875,

10 China

11 ²State Key Laboratory of Atmospheric Boundary Layer Physics and Atmospheric Chemistry,

12 Institute of Atmospheric Physics, Chinese Academy of Sciences, Beijing 100029, China

13 ³College of Earth Sciences, University of Chinese Academy of Sciences, Beijing 100049, China

14 ⁴Key Laboratory of Regional Numerical Weather Prediction, Institute of Tropical and Marine

15 Meteorology, China Meteorological Administration, Guangzhou 510080, China

16 ⁵Shared Experimental Education Center, Sun Yat-sen University, Guangzhou 510275, China

17 ⁶Collaborative Innovation Center on Forecast and Evaluation of Meteorological Disasters, Nanjing

18 University of Information Science and Technology, Nanjing, 210044, China

19

20 **Correspondence to: Zhanqing Li (zli@atmos.umd.edu)*

21

22 **Abstract**

23

24 This study investigates aerosol hygroscopicity, mixing state, and cloud condensation
25 nucleation as part of the Atmosphere-Aerosol-Boundary Layer-Cloud Interaction Joint
26 Experiment done in the summer of 2016 at Xingtai (XT), a suburban site located in
27 the center of the North China Plain (NCP). In general, the probability density function
28 (PDF) of the hygroscopicity parameter (κ) for 40–200-nm particles had a unimodal
29 distribution, and mean κ -PDF patterns for different sizes were similar, suggesting that
30 the particles were highly aged and internally mixed because of strong photochemical
31 reactions. The κ calculated from the hygroscopic growth factor in the daytime and at
32 night suggests that photochemical reactions largely enhanced the aerosol
33 hygroscopicity. This effect became weaker as the particle size increased. In addition,
34 the aerosol hygroscopicity was much larger at XT than at other sites in the NCP. This
35 is because new particle formation takes place much more frequently in the central
36 NCP, which is heavily polluted from industrial activities, than elsewhere in the region.
37 The evolution of the planetary boundary layer played a dominant role in dictating
38 aerosol mass concentration. Particle size was the most important factor influencing
39 the ability of aerosols to activate, whereas the effect of chemical composition was
40 secondary, especially when supersaturation was high. Using a fixed value of $\kappa =$
41 0.31 to calculate the cloud condensation nuclei number concentration in this region
42 suffices.

43 **1. Introduction**

44 Aerosols, defined as the mixture of solid and liquid particles suspended in air, are
45 ubiquitous in the atmosphere because of direct emissions from biogenic and
46 anthropogenic sources, and the secondary transformation from gas precursors. Aerosol
47 particles play an important role in climate change through direct and indirect effects
48 (e.g., Ramanathan et al., 2001; Rosenfeld et al., 2008; Li et al., 2016). However, the
49 impact of aerosols on climate change is difficult to simulate because of the highly
50 variable physical and chemical properties of aerosols, and complex aerosol-cloud
51 interactions (IPCC, 2013; Lebo et al., 2017).

52 The hygroscopic growth and mixing state of aerosol particles are important for
53 estimating the direct radiative effect of aerosols on Earth's climate. This is because
54 the growth and mixing can change the particle size and optical properties of aerosol
55 particles which influences the solar radiation budget and atmospheric visibility. In
56 addition, aerosol particles can be activated as cloud condensation nuclei (CCN) under
57 supersaturation (SS) conditions. The variability in CCN number concentration (N_{CCN})
58 can modify both cloud microphysical properties (Twomey, 1974; Albrecht, 1989) and
59 morphology (Rosenfeld et al., 2008) and can lead to a broad impact on a wide range
60 of meteorological variables including severe weather events (Li et al., 2017a).

61 Previous studies have addressed three main aerosol properties influencing the
62 CCN activation, namely, particle size, chemical composition, and mixing state.
63 However, their relative importance is different under different environmental

64 conditions (e.g., Dusek et al., 2006; Ervens et al., 2007; Cubison et al., 2008; Deng et
65 al., 2011; Zhang et al., 2014; Schmale et al., 2018).

66 Ambient aerosols are composed of different species, including inorganic ions,
67 organic components, black carbon (BC), and mineral dust. Inorganics mainly contain
68 sulfate, nitrate, and ammonium, while organic aerosols (OA) consist of thousands of
69 chemicals (Jacobson et al., 2000). The hygroscopicity and CCN activity of a single
70 component can be characterized according to laboratory studies (e.g., Petters and
71 Kreidenweis, 2007), but the properties of their mixtures are hard to estimate because
72 of the different chemical species and mixing states of particles in the atmosphere.
73 Therefore, aerosol hygroscopicity and CCN activity are very different in different
74 regions due to different chemical compositions. Comprehensive field measurements
75 of aerosol properties in different regions are thus necessary to improve models.

76 China, especially the North China Plain (NCP), has been suffering from severe air
77 pollution over the last couple of decades due to rapid industrialization and
78 urbanization. Diverse sources and aging processes make aerosol properties
79 particularly diverse and complex in this part of the world. As such, the region has
80 drawn much attention regarding the aerosol mixing state, hygroscopicity, and CCN
81 activity (Deng et al., 2011; Liu et al., 2011; Zhang et al., 2014; F. Zhang et al., 2016;
82 S.L. Zhang et al., 2016; Wu et al., 2016; Y. Wang et al., 2017). Liu et al. (2011) and
83 Y. Wang et al. (2017) have suggested that ambient particles are mostly an external
84 mixture with different hygroscopicities. Deng et al. (2011) have shown that the
85 aerosol number size distribution is critical in the prediction of N_{CCN} while Zhang et al.

86 (2014, 2017) have highlighted the importance of chemical composition in determining
87 particle activation properties. However, these studies were done using data from the
88 northern part of the NCP. Few studies have focused on the central region of the NCP.
89 Compared to the northern part of the NCP, the central part of the NCP is more affected
90 by industrial emissions because a dense cluster of China's heavy industries exists
91 there (Fu et al., 2014). Measurements of aerosol properties in the central part of the
92 NCP are thus critically needed to investigate the impact of air pollution on the
93 environment and climate change.

94 Xingtai (XT), a city located in the center of the NCP, is considered one of the
95 most polluted cities in China. Local industrial and domestic sources of pollution are
96 the greatest contributors to severe haze events in that region (Wang et al., 2014). A
97 field experiment called the Atmosphere-Aerosol-Boundary Layer-Cloud (A²BC)
98 Interaction Joint Experiment was done at a suburban site in XT in the summer of 2016.
99 Differences in aerosol properties at this site and at sites in the northern part of the
100 NCP were found.

101 The paper is organized as follows. Sections 2 and 3 describe the measurement
102 method and data analysis theory. Section 4 presents and discusses the measurement
103 results, which includes data time series, aerosol mixing state, hygroscopicity, CCN
104 prediction and its sensitivity to chemical composition. A summary and conclusions are
105 given in section 5.

106 **2. Measurements**

107 **2.1. Sampling site and meteorology**

108 The A²BC experiment was done at the National Meteorological Basic Station
109 located in XT (37.18°N, 114.37°E, 180 m above sea level) from 1 May to 15 June of
110 2016. This suburban site is situated ~17 km northwest of the XT urban area in
111 southern Heibei Province, which is located in the central part of the NCP and to the
112 east of the Taihang Mountains (Fig. 1a). This region is heavily populated, urbanized,
113 and industrialized. Major industrial manufacturers include coal-based power plants,
114 steel and iron works, glassworks, and cement mills. Weak diffusion conditions and
115 heavy industrial emissions lead to exceptionally high concentrations of particulate
116 matter (PM) with diameters less than 10 μm and 2.5 μm (PM_{2.5}), as well as gas
117 pollutants such as sulfur dioxide (SO₂), volatile organic compounds (VOCs), and
118 nitrogen oxides (NO_x) during the frequently occurring haze episodes in this region
119 (Wang et al., 2014; Fu et al., 2014). Figure 1b shows the mean distribution of SO₂
120 concentrations from May of 2012 to 2016 which confirms that the measurement site is
121 located in one of the pollution centers in this region. A detailed analysis of gas
122 precursors and aerosol chemical species shows that this station is a representative site
123 in this region (Zhang et al., 2018).

124 Time series of meteorological variables measured at this meteorological station
125 are shown in Fig. S1. This site is strongly affected by mountain-valley winds.
126 Southeasterly winds prevail during the day and at night northwesterly winds prevail

127 (Fig. S1 and Fig. S2). There was almost no precipitation during the study period. The
128 ambient temperature (T) and relative humidity (RH) time series show opposing trends.
129 Campaign-mean values of T and RH are 21.9°C and 51.6%, respectively.

130 **2.2. Instrumentation and operation**

131 **2.2.1. Aerosol hygroscopicity measurements**

132 The custom-built hygroscopicity tandem differential mobility analyzer (HTDMA)
133 used in this study has been described in detail by others (Tan et al., 2013; Y. Wang et
134 al., 2017). Briefly, ambient aerosols are first dried and neutralized by a Nafion dryer
135 and a soft X-ray charger. A differential mobility analyzer (DMA₁, model 3081L, TSI
136 Inc.) is used to select monodispersed particles of a certain diameter. The
137 monodispersed particles are then passed through a Nafion humidifier with a controlled
138 higher RH and are humidified. A second DMA (DMA₂, same model as the DMA₁)
139 and a water-based condensation particle counter (WCPC, model 3787, TSI Inc.) are
140 used to measure the number size distribution of the humidified particles. The DMA₁
141 and WCPC can also be connected directly to measure the 10–400-nm particle number
142 size distribution (PNSD). In this study, the dry diameters selected by the DMA₁ were
143 40, 80, 110, 150, and 200 nm, and the humidified RH was set to 85%. The RH
144 calibration with ammonium sulfate for the H-TDMA is shown in Fig. S3.

145 The hygroscopic growth factor (GF) is defined as the ratio of the humidified
146 diameter at a given RH to the dry diameter:

$$147 \quad GF = \frac{D_p(\text{RH})}{D_{p0}}, \quad (1)$$

148 where $D_p(\text{RH})$ is the particle diameter at the given RH and D_{p0} is the dry diameter
149 selected by the DMA₁. The measured distribution function versus GF can be
150 calculated with WCPC data downstream from the DMA₁ and DMA₂. The GF
151 probability density function is then retrieved using the TDMAFIT algorithm
152 (Stolzenburg and McMurry, 1988, 2008).

153 **2.2.2. Aerosol chemical composition measurements**

154 An Aerosol Chemical Speciation Monitor (ACSM) was used to measure
155 non-refractory submicron aerosol species (sulfate, nitrate, ammonium, chloride, and
156 organics) in real-time. A PM_{2.5} URG cyclone (model URG-2000-30ED) was installed
157 in the front of the sampling inlet to remove coarse particles ($> 2.5 \mu\text{m}$ in diameter).
158 Before sampling into the ACSM, aerosol particles were dried (below 40% RH) by a
159 silica gel diffusion dryer. The ACSM was calibrated routinely with pure ammonium
160 nitrate to determine its ionization efficiency. More detailed descriptions about the
161 ACSM are given by Ng et al. (2011) and Sun et al. (2012). A positive matrix factor
162 analysis was used to analyze the organic spectral matrices according to Ulbrich et al.
163 (2009). Three factors, i.e., hydrocarbon-like OA (HOA), cooking OA (COA), and
164 oxygenated OA (OOA), are chosen as the ACSM dataset. HOA and COA are both
165 primary organic aerosols (POA) while OOA is the secondary organic aerosol (SOA).

166 The ACSM does not detect refractory material such as BC, so a seven-wavelength
167 aethalometer (AE-33, Magee Scientific Corp.) with a PM with diameters less than 1
168 μm (PM₁) cyclone was used to measure the BC mass concentration of BC particles

169 with diameters $< 1.0 \mu\text{m}$. Mineral dust and sea salt are the other refractory species, but
170 they typically exist in the coarse mode and contribute negligibly to PM_1 (Juranyi et al.,
171 2010; Meng et al., 2014).

172 **2.2.3. Aerosol size distribution and CCN measurements**

173 The aerosol particle number size distribution (15–685 nm) was measured by a
174 scanning mobility particle sizer (SMPS) that was equipped with a long DMA (model
175 3081L, TSI Inc.) and a condensation particle counter (model 3775, TSI Inc.). A
176 single-column continuous-flow thermal-gradient cloud condensation nuclei counter
177 (model CCNC-100, DMT Inc.) was used to measure the bulk CCN number
178 concentration. Five SS levels, i.e., 0.07, 0.1, 0.2, 0.4, and 0.8%, were set in the CCNC
179 and the running time was 10 min for each SS level. The SS levels in the CCNC were
180 calibrated with pure ammonium sulfate (Rose et al., 2008) before and after the
181 measurement campaign. The corrected SS levels were 0.11, 0.13, 0.22, 0.40, and
182 0.75%.

183 The aerosol activation ratio (AR) at a certain SS is calculated as N_{CCN} divided by
184 the total particle number concentration in the 15–685-nm range ($N_{15-685 \text{ nm}}$), i.e., $\text{AR} =$
185 $N_{\text{CCN}} / N_{15-685 \text{ nm}}$. The SMPS does not measure particle number concentrations below
186 15 nm. Since the activation critical diameter is always larger than 15 nm at these SS
187 levels (Zhang et al., 2014), this does not affect the calculated N_{CCN} . Aerosol particles
188 with diameters greater than 685 nm are also not detected by the SMPS. These larger
189 particles will always act as CCN due to their larger dry sizes. Note that the number

190 concentration above 685 nm in the atmosphere is always negligible (Juranyi et al.,
191 2010).

192 **2.2.4. Other measurements**

193 In this study, a micro-pulse lidar (MPL-4B, Sigmaspace Corp.) was used to study
194 the evolution of the planetary boundary layer (PBL) which plays a crucial role in
195 modulating surface air quality (Z. Li et al., 2017b). The pulse repetition rate of the
196 MPL was 2.5 kHz at a visible wavelength of 532 nm. The peak value of the optical
197 energy of the laser beam was 8 μ J. The pulse duration ranged from 10 to 100 ns, and
198 the pulse interval was set to 200 ns, corresponding to a spatial resolution of 30 m. The
199 MPL-retrieved PBL height is the altitude where a sudden decrease in the scattering
200 coefficient occurs (Brooks, 2003; Quan et al., 2013). Trace gas analyzers
201 (manufactured by ECOTECH) were used to measure the gaseous species of ozone,
202 SO₂, NO_x, NO, and carbon monoxide. More detailed descriptions about the analyzers
203 are given by Zhu et al. (2016).

204 Two containers at ground level housed all sampling instruments. Two air
205 conditioners maintained the temperature at 20–25°C inside the containers. All
206 stainless tube inlets were ~1.5 m above the top of the containers.

207 **3. Theory**

208 **3.1. Hygroscopicity parameter**

209 To link hygroscopicity measurements below and above the water vapor saturation,

210 the Köhler theory (Köhler, 1936) is parameterized using the hygroscopicity parameter
 211 κ (Petters and Kreidenweis, 2007). This is known as the κ -Köhler theory. According
 212 to the theory, the equilibrium equation for a solution droplet at a saturation ratio $S(D)$
 213 is

$$214 \quad S(D) = \frac{D^3 - D_d^3}{D^3 - D_d^3(1 - \kappa)} \exp\left(\frac{4\sigma_{s/a}M_w}{RT\rho_w D}\right) \quad , \quad (2)$$

215 where D and D_d are the wet and dry droplet diameters, respectively, $\sigma_{s/a}$ is the
 216 surface tension coefficient, M_w is the mole mass of water, R is the universal gas
 217 constant, T is the temperature, and ρ_w is the density of water.

218 Below the water vapor saturation, $S(D)$ is RH, D is $D_p(\text{RH})$, and D_d is D_{p0}
 219 from Eq. (1). The κ parameter is then calculated using H-TDMA data according to Eq.
 220 (1) and Eq. (2):

$$221 \quad \kappa_{\text{gf}} = (\text{GF}^3 - 1) \cdot \left[\frac{1}{\text{RH}} \exp\left(\frac{4\sigma_{s/a}M_w}{RT\rho_w D_d \text{GF}}\right) - 1 \right] \quad . \quad (3)$$

222 For a multicomponent particle, the Zdanovskii–Stokes–Robinson (ZSR) mixing
 223 rule (Stokes and Robinson, 1966) can also estimate κ using chemical composition
 224 data:

$$225 \quad \kappa_{\text{chem}} = \sum_i \varepsilon_i \kappa_i, \quad (4)$$

226 where ε_i and κ_i are the volume fraction and κ for the i th chemical component,
 227 respectively. The ACSM provides the mass concentrations of inorganic ions and
 228 organics. A simplified ion-pairing scheme such as that described by Gysel et al. (2007)
 229 is applied to convert ion mass concentrations to mass concentrations of their
 230 corresponding inorganic salts (see Table S1 in the supplement). Table S1 also lists κ
 231 and the gravimetric density of each individual component under supersaturated

232 conditions. In the following discussions, κ_{gf} and κ_{chem} denote the hygroscopicity
233 parameters derived from H-TDMA measurements and estimated using the ZSR
234 mixing rule, respectively.

235 **3.2. CCN estimation**

236 The critical supersaturation (s_c , $s_c = S_c - 1$) for the D_d of a particle with
237 hygroscopicity κ is calculated from the maximum of the κ -Köhler curve (Eq. 2;
238 Petters and Kreidenweis, 2007). The D_d is also the critical diameter corresponding to
239 the s_c when κ is known. The s_c - D_d relationship can thus be established. According to
240 this relationship, the critical diameter ($D_{0,\text{crit}}$) can be calculated using the estimated
241 κ_{chem} (Eq. 4) at a given SS. All particles larger than $D_{0,\text{crit}}$ will activate as CCN,
242 assuming that aerosols are internally mixed. Then the CCN number concentration can
243 be estimated from the integral of the aerosol size distribution provided by the SMPS
244 from $D_{0,\text{crit}}$ to the maximum measured size (D_{max}):

$$245 \quad N_{\text{CCN}}(\text{SS}) = \int_{D_{0,\text{crit}}(\text{SS})}^{D_{\text{max}}} \frac{dN(D)}{d\log(D)} d\log(D) . \quad (5)$$

246 $N_{\text{CCN}}(\text{SS})$ can then be compared to the number of CCN at the same SS measured by
247 the CCNC.

248 **4. Results and discussion**

249 **4.1. Overview**

250 Figures 2 and 3 show time series of the main aerosol properties measured during
251 the field campaign. The PNSD changes dramatically (Fig. 2a) and the aerosol number

252 concentration in the 15–50 nm range ($N_{15-50 \text{ nm}}$) increases sharply in the morning
253 almost every day (Fig. 2b). The time series of the mean diameter (D_m) of particles also
254 shows that a growth process occurs after the sharp increase in $N_{15-50 \text{ nm}}$. All these
255 phenomena suggest that new particle formation (NPF) events frequently occurred at
256 XT during the field experiment (Kulmala et al., 2012; Y. Li et al., 2017). This is likely
257 related to the high concentration of gas precursors from mainly local emissions. High
258 emissions of SO_2 and VOCs associated with the high oxidation capacity in a polluted
259 atmosphere make NPF events occur more frequently in northern China (Z. Wang et al.,
260 2017).

261 Figure 2c-d shows time series of the probability density functions (PDFs) of κ_{gf}
262 (κ -PDF) for 40-nm and 150-nm particles, respectively. In general, mono-modal
263 κ -PDFs were observed. This is different from κ -PDFs at other sites in China where
264 bi- and tri-modal distributions dominate (Liu et al., 2011; Ye et al., 2013; Jiang et al.,
265 2016; S. L. Zhang et al., 2016; Y. Wang et al., 2017). Differences in the aerosol
266 mixing state explain this (see section 4.2).

267 Figure 3a shows the bulk mass concentrations of organics, sulfate, nitrate,
268 ammonium, and chloride measured by the ACSM and the BC mass concentration
269 measured by the AE-33. Organics and sulfate were the dominant chemical species
270 with mass fractions in PM_{10} of 39.1% and 24.7%, respectively. Figure 3b-c shows the
271 volume fractions of paired chemical compositions and κ_{chem} , respectively. The average
272 volume fraction of inorganics ($(\text{NH}_4)_2\text{SO}_4 + \text{NH}_4\text{HSO}_4 + \text{H}_2\text{SO}_4 + \text{NH}_4\text{NO}_3$) was similar
273 to that of organics (POA+SOA), but their volume fractions changed diurnally. In

274 general, the volume fraction of inorganics increased during daytime while the volume
275 fraction of organics decreased. SOA was the dominant contributor to OA, accounting
276 for ~69% of the organics volume. This shows that photochemical reactions were
277 strong at XT during the field campaign (Huang et al., 2014). The mean κ_{chem} in Fig.
278 3c was 0.31 with values ranging from 0.20 to 0.40. The trend in κ_{chem} was similar to
279 that of the volume fraction of inorganics. This suggests that inorganics played a key
280 role in κ_{chem} . This is consistent with the study by Wu et al. (2016).

281 **4.2. Aerosol mixing state and hygroscopicity**

282 Figure 4 shows mean κ -PDFs for different particle sizes derived from H-TDMA
283 data. For all particle sizes considered, κ_{gf} ranged from 0 to 0.8, and the κ -PDF
284 patterns were similar. This suggests that hygroscopic compounds in different particle
285 size modes were similar at XT. In general, κ -PDF patterns show only one hydrophilic
286 mode with a weak hydrophobic mode occasionally appearing at night when
287 photochemical reactions are weak (Fig. S4). The κ -PDF patterns always show bi- or
288 tri-modal distributions at other sites in China (Liu et al., 2011; Ye et al., 2013; Jiang et
289 al., 2016; Zhang et al., 2016; Y. Wang et al., 2017). Based on previous studies (Liu et
290 al., 2011; Y. Wang et al., 2017), ambient aerosols can be classified into three groups
291 according to their κ_{gf} values:

292 — nearly hydrophobic (NH): $\kappa_{\text{gf}} < 0.1$

293 — less hygroscopic (LH): $0.1 \leq \kappa_{\text{gf}} < 0.2$

294 — more hygroscopic (MH): $0.2 \leq \kappa_{\text{gf}}$

295 Table 1 gives the number fractions of each group for different particle sizes. The MH
296 group dominated all particle sizes. The number fractions of the NH and LH groups
297 were both less than 6.0%. However, the volume fractions of hydrophobic BC and
298 low-hygroscopic organics (where κ_{BC} is approximately zero and κ_{organic} is
299 typically less than 0.1) were ~10.1% and 47.4%, respectively, according to chemical
300 composition measurements (Fig. 3b). This suggests that the particles were highly aged
301 and internally mixed at XT during the field campaign. The coating of sulfates and
302 secondary organics during the aging process changes the structure of BC and makes
303 these particles grow which can significantly enhance the hygroscopicities of particles
304 (e.g., Zhang et al., 2008; Jimenez et al., 2009; Tritscher et al., 2011; Guo et al., 2016).
305 The observed unimodal distribution of κ -PDF also suggests the internal mixing state
306 of the particles (Swietlicki et al., 2008).

307 Figure 5 shows the average size-resolved κ_{gf} derived from H-TDMA data at XT
308 and other sites in China. At XT, κ_{gf} for different particle sizes were larger in the
309 daytime than at night, and the difference between daytime and nighttime decreased
310 with increasing particle size. This suggests that the impact of photochemical reactions
311 on aerosol hygroscopicity is strong. The effect is weaker with increasing particle size
312 because most of the larger particles are always well aged.

313 The magnitude of κ_{gf} was larger at XT than at other sites in China. In particular,
314 the magnitude of κ_{gf} was much larger at XT than at sites in the northern part of the
315 NCP, i.e., Beijing, Wuqing, and Xianghe. The lower κ_{gf} in the Beijing urban area is
316 likely related to the more severe traffic emissions there (Ye et al., 2013; Wu et al.,

317 2016). Wuqing and Xianghe are located in the suburban area between the two
318 megacities of Beijing and Tianjin and are simultaneously affected by traffic and
319 industrial emissions. The magnitudes of κ_{gf} at these two sites are higher than at
320 Beijing but lower than at XT. Although distant from these megacities, XT is situated
321 in the industrial center of the NCP, so particles there are more internally mixed and
322 highly aged due to the higher concentrations of precursors and strong photochemical
323 reactions. This is why κ_{gf} at XT is larger than at other sites. This suggests that the
324 hygroscopicities of particles from different emissions and chemical processes differ in
325 the NCP. Forty nm particles were always more hygroscopic than 80-nm particles at
326 XT, especially in the daytime. This differed from other sites likely because the coating
327 effect of sulfates and secondary organics is more significant for smaller particles
328 (Tritscher et al., 2011; Guo et al., 2016). Furthermore, since the field measurements
329 took place in a locality with heavy industrial activities, it is possible that amine
330 contributed significantly to the hygroscopicity of 40-nm particles. Several studies
331 have shown that amine compounds in aerosol phase can be hygroscopic, sometimes at
332 even low RH (e.g., Qiu and Zhang, 2012; Chu et al., 2015; Gomez-Hernandez et al.,
333 2016).

334 **4.3. Diurnal variations in aerosol properties**

335 **4.3.1. Diurnal variations in aerosol number and mass concentrations**

336 Figure 6a shows the diurnal variation in MPL-derived PBL height. The PBL
337 height is the altitude where a sudden decrease in the MPL-measured scattering

338 coefficient occurs (Cohn and Angevine, 2000; Brooks, 2003). Note that the retrieved
339 PBL height is only valid from 0700 local time (LT) to 1900 LT (Quan et al., 2013).
340 The retrieved PBL height at night is not accurate because of the likely influence of
341 residual aerosols within the nocturnal PBL. The evolution of PBL height from 0700
342 LT to 1900 LT is sufficient to analyze its link with the change in aerosol number and
343 mass concentrations during the daytime. Figure 6b shows diurnal variations in aerosol
344 number and mass concentrations in the 15–685 nm range ($N_{15-685 \text{ nm}}$ and $\text{PM}_{15-685 \text{ nm}}$,
345 respectively). Variations in $N_{15-685 \text{ nm}}$ and $\text{PM}_{15-685 \text{ nm}}$ trended opposite from each other.
346 From 0800 LT to 1400 LT, the PBL height lifted from ~0.5 km to ~0.6 km, while
347 $\text{PM}_{15-685 \text{ nm}}$ generally decreased from ~24 $\mu\text{g m}^{-3}$ to ~19 $\mu\text{g m}^{-3}$. This suggests the
348 important effect of PBL evolution on $\text{PM}_{15-685 \text{ nm}}$. However, $N_{15-685 \text{ nm}}$ sharply
349 increased from ~7600 cm^{-3} at 0700 LT to ~13,000 cm^{-3} at 1300 LT. This is related to
350 the sudden burst of small Aitken-mode particles (< 50 nm) during NPF events. Newly
351 formed fine particles contribute little to $\text{PM}_{15-685 \text{ nm}}$. In the evening, $\text{PM}_{15-685 \text{ nm}}$
352 increased gradually while $N_{15-685 \text{ nm}}$ decreased. The decline of the nocturnal PBL and
353 particle coagulation and growth explains this. In other words, the evolution of the
354 PBL influenced the aerosol mass concentration, while particle formation and growth
355 had a greater influence on the variation in aerosol number concentration.

356 **4.3.2. Diurnal variation in aerosol hygroscopicity**

357 Figure 6c shows diurnal variations in κ_{gf} and κ_{chem} . Values of κ_{gf} for different
358 particle sizes increased in the morning when the NPF event started. The increase was

359 sharpest for 40-nm particles. The increase in κ_{gf} in the morning synchronized with
360 the particle number concentration ($N_{15-685 \text{ nm}}$) but not with the PBL height, further
361 suggesting the impact of photochemical reactions on aerosol hygroscopicity. The κ_{gf}
362 for 40-nm particles increased from ~ 0.32 at 0700 LT to ~ 0.44 at 1500 LT and
363 approached the κ value of pure ammonium sulfate. This also suggests that a large
364 amount of hygroscopic compounds were produced during NPF events. Fig. S5 shows
365 sharply increased concentrations of SO_2 and VOCs in the morning and the enhanced
366 atmospheric oxidation capacity under high RH and low T conditions. The production
367 of sulfate and SOAs resulted. This is why aerosol hygroscopicity and the occurrence
368 of NPF events increased. Zhang et al. (2018) characterized the aerosol chemistry
369 during NPF events in this field campaign. The diurnal pattern in κ_{gf} for 80–200 nm
370 particles differs from that of 40-nm particles. The differences in κ_{gf} for 80–200 nm
371 particles in the early morning were large but gradually decreased as the sun rose. The
372 κ_{gf} for 80–200-nm particles were similar but lower than that for 40-nm particles after
373 1100 LT. The condensation of sulfates and secondary organics likely caused the
374 enhanced hygroscopicity of the 40–200-nm particles, especially of 40-nm particles
375 (Fig. 6d).

376 Figure 6c also shows that the κ_{chem} for PM_{10} was lower than the κ_{gf} for 40–
377 200-nm particles and had a weaker diurnal variation. This feature was stronger at
378 noon when atmospheric oxidation and the aging process were more rapid. The simple
379 ZSR mixing rule is responsible for this. During the daytime, the condensation of
380 sulfuric acid on organics or BC greatly enhances their hygroscopicities (Zhang et al.,

381 2008; Zhang et al., 2017). The ZSR model cannot accurately represent this
382 phenomenon. Cruz and Pandis (2000) have shown that the measured κ_{gf} of internally
383 mixed $(\text{NH}_4)_2\text{SO}_4$ -organic aerosols is larger than the predicted κ_{chem} based on the
384 ZSR model.

385 In summary, the ample supply of SO_2 and VOCs provided sufficient precursors
386 for the strong photochemical reactions at XT during this field campaign, and the
387 production and condensation of sulfate and SOAs greatly enhanced aerosol
388 hygroscopicity, especially during the daytime. The oxidation of precursors likely
389 induced the observed frequent NPF events.

390 **4.3.3. Diurnal variation in CCN number concentration and activation ratio**

391 Figure 7a shows the diurnal variations in N_{CCN} and AR at different SS. In the
392 morning, N_{CCN} first decreased then increased while AR showed the opposite trend.
393 This is related to the evolution of the PBL and NPF events. At the initial stage of an
394 NPF event, the newly formed particles were less than 15 nm in size which was below
395 the detection limit of the SMPS. As a result, $N_{15-685 \text{ nm}}$ decreased (Fig. 6b) as the PBL
396 lifted, and N_{CCN} also decreased. However, the mixing of aged particles within the PBL
397 made the particle size (Fig. 7b) and AR increase slightly. Condensation and the
398 growth of new particles caused the number of fine particles detected by the SMPS to
399 increase rapidly. However, because of their smaller sizes, some of these particles were
400 not activated. Therefore, N_{CCN} increased, but AR decreased from 0800 LT to 1400 LT.
401 In the afternoon and evening, N_{CCN} and AR increased slightly as particle sizes

402 increased (Fig. 7b). These trends weakened as SS decreased because the critical
403 diameter is larger at low SS and the influence of aerosol size distribution on N_{CCN} and
404 AR is relatively weaker. Particle size was the most important factor influencing
405 aerosol activation and CCN number concentrations, especially at larger SS. Figure 6S
406 shows the results from a sensitivity test of particle size in a CCN closure study similar
407 to that done by Dusek et al. (2006).

408 **4.4. CCN estimation from chemical composition data**

409 This section presents a CCN closure study and a discussion of the impact of
410 chemical composition on N_{CCN} . It is reasonable to assume that aerosols are internally
411 mixed when estimating N_{CCN} because H-TDMA data showed that this was the case at
412 XT. Figure 8a shows estimated N_{CCN} as a function of measured N_{CCN} using real-time
413 κ_{chem} . The estimated N_{CCN} correlates well with measurements ($R^2 \geq 0.85$), but is
414 generally overestimated. The slope of each linearly fitted line is greater than 1.10 and
415 increases with increasing SS. The relative deviation (RD) increases from 16.2% to
416 25.2% as SS increases from 0.13% to 0.75%, suggesting that estimates become worse
417 at larger SS. The large measurement uncertainties of CCNC mainly cause the
418 overestimation of N_{CCN} : (1) The temperature or high flow rates in the CCNC may not
419 allow enough time for particles to reach sizes large enough to be counted by the
420 optical particle counter at the exit of the CCN chamber (Lance et al., 2006; Cubison et
421 al., 2008) and (2) in high particle number concentration environments, water depletion
422 in the CCNC may reduce the counting rate of the CCNC (Deng et al., 2011). These

423 uncertainties make measured N_{CCN} lower than the actual N_{CCN} . At larger SS, activated
424 aerosols in the cloud chamber of the CCNC are greater in number and smaller in size,
425 so the impact of these uncertainties is greater. Figure S7 shows results from the N_{CCN}
426 closure study for separated N_{CCN} . The CCN closure is reasonable when $N_{CCN} < 5500$
427 cm^{-3} .

428 Figure 8b shows estimated N_{CCN} using the mean value for κ_{chem} ($\kappa_{\text{chem}} = 0.31$).
429 Compared with results using real-time values for κ_{chem} , the fit parameters and RD
430 change slightly, suggesting that the effect of chemical composition on N_{CCN} is weaker
431 relative to the particle size. Figure 9 shows the sensitivity of estimated N_{CCN} to the
432 variability in chemical composition. The variability in the equipotential lines of RD
433 suggests that the sensitivity of N_{CCN} is strongly time dependent. This is attributed to
434 the variability of the shape of the aerosol size distribution (Juranyi et al., 2010) which
435 further demonstrates the importance of particle size to N_{CCN} . The sensitivity of N_{CCN}
436 to chemical composition (κ_{chem}) becomes weaker with increasing SS, suggesting that
437 chemical composition becomes less important in N_{CCN} estimates at larger SS. RD is
438 always less than 10% when estimating N_{CCN} using the mean value of κ_{chem} . The
439 value $\kappa = 0.31$ is thus a good reference value to model N_{CCN} in this region.

440 In summary, the particle size is the most important factor influencing aerosol
441 activation at XT, especially at larger SS. The chemical composition was not as
442 important when estimating N_{CCN} because particles were highly aged and internally
443 mixed at XT. Aerosol hygroscopicity was not sensitive to estimates of N_{CCN} .

444 5. Summary and conclusions

445 The Atmosphere-Aerosol-Boundary Layer-Cloud (A²BC) Interaction Joint
446 Experiment was done at a suburban site (Xingtai, or XT) located in the central North
447 China Plain (NCP) from 1 May to 15 June of 2016. The study investigated aerosol
448 hygroscopicity, the mixing state, and CCN activity at XT.

449 In general, the probability density function (PDF) of the hygroscopicity parameter
450 κ (κ -PDF) for 40–200-nm particles was a unimodal distribution, which is different
451 from distributions at other sites in China. Particles of all sizes covered a large range of
452 κ_{gf} (the hygroscopicity parameter derived from H-TDMA measurements; mostly
453 from 0 to 0.8) and showed similar κ -PDF patterns, suggesting that the hygroscopic
454 compounds in these particles from 40 nm to 200 nm were similar at XT. The κ -PDF
455 patterns also suggest that particles were highly aged and internally mixed at XT
456 during the field campaign. This is likely related to strong photochemical reactions.

457 The mean κ_{gf} for different particle sizes were larger in the daytime than at night.
458 Daytime and nighttime κ_{gf} differences decreased with increasing particle size. The
459 impact of photochemical reactions on aerosol hygroscopicity was strong, and the
460 effect became weaker as particle size increased. The coating of sulfates or secondary
461 organics likely enhanced the hygroscopicities of 40–200-nm particles. This effect was
462 more significant for 40-nm particles. Compared with other sites in China, the aerosol
463 hygroscopicity was much larger at XT because of the sufficient amount of precursors
464 and strong atmospheric oxidation. The comparison also shows that the

465 hygroscopicities of particles from different emissions and chemical processes differed
466 greatly.

467 New particle formation events occurred frequently at XT during this field
468 campaign. The evolution of the planetary boundary layer influenced the aerosol mass
469 concentration, while particle formation and growth had a greater influence on the
470 variation in aerosol number concentration. Particle size was the most important factor
471 influencing aerosol activation and the CCN number concentration (N_{CCN}) at XT,
472 especially at larger supersaturations (SS). Although estimated N_{CCN} correlated well
473 with measurements ($R^2 \geq 0.85$), N_{CCN} was overestimated because of measurement
474 uncertainties. The effect of chemical composition on N_{CCN} was weaker relative to the
475 particle size. Sensitivity tests show that the impact of chemical composition on N_{CCN}
476 became weaker as SS increased, suggesting that the effect of chemical composition on
477 the estimation of N_{CCN} is less important at larger SS. The value $\kappa = 0.31$ is a good
478 proxy for N_{CCN} in this region.

479 XT is located in the most polluted region in China. The multitude of factories in the
480 region generates strong emissions. The plenitude of gas precursors and strong
481 photochemical reactions at XT make aerosol properties there unique. More field
482 measurements on gas-particle transformation and aerosol properties in this region are
483 needed for studying haze formation mechanisms and climate effects.

484
485 *Data availability.* Data used in the study are available from the first author upon
486 request (wang.yuying@mail.bnu.edu.cn).

487
488 *Competing interests.* The authors declare that they have no conflict of interest.

489

490 *Author contribution.* Z. L. and Y. W. designed the experiment; Y. W., Y. Z., and W. D.
491 carried it out and analyzed the data; other co-authors participated in science discussions
492 and suggested analyses. Y. W. prepared the manuscript with contributions from all
493 co-authors.

494
495 *Acknowledgements.* This work was funded by National Natural Science Foundation of
496 China (NSFC) research projects (grant no. 91544217, 41675141, 41705125), the
497 National Basic Research Program of China “973” (grant no. 2013CB955801), and the
498 China Scholarship Council (award no. 201706040194). We thank all participants in
499 the field campaign for their tireless work and cooperation.

500

501 **References**

- 502 Albrecht, B. A.: Aerosols, cloud microphysics, and fractional cloudiness, *Science*, 245,
503 1227–1230, <https://doi.org/10.1126/science.245.4923.1227>, 1989.
- 504 Brooks, I. M.: Finding boundary layer top: application of a wavelet covariance
505 transform to lidar backscatter profiles, *J. Atmos. Ocean. Tech.*, 20, 1092–1105,
506 [https://doi.org/10.1175/1520-0426\(2003\)020<1092:FBLTAO>2.0.CO;2](https://doi.org/10.1175/1520-0426(2003)020<1092:FBLTAO>2.0.CO;2), 2003.
- 507 Chu, Y., Sauerwein, M., and Chan, C. K.: Hygroscopic and phase transition properties
508 of alkyl aminium sulfates at low relative humidities, *Phys. Chem. Chem. Phys.*, 17,
509 19,789–19,796, <https://doi.org/10.1039/c5cp02404h>, 2015.
- 510 Cohn, S. A., and Angevine, W. M.: Boundary layer height and entrainment zone
511 thickness measured by lidars and wind-profiling radars, *J. Appl. Meteorol.*, 39,
512 1233–1247,
513 [https://doi.org/10.1175/1520-0450\(2000\)039<1233:BLHAEZ>2.0.CO;2](https://doi.org/10.1175/1520-0450(2000)039<1233:BLHAEZ>2.0.CO;2), 2000.
- 514 Cruz, C. N., and Pandis, S. N.: Deliquescence and hygroscopic growth of mixed
515 inorganic–organic atmospheric aerosol, *Environ. Sci. Technol.*, 34, 4313–4319,
516 <https://doi.org/10.1021/es9907109>, 2000.
- 517 Cubison, M. J., Ervens, B., Feingold, G., Docherty, K. S., Ulbrich, I. M., Shields, L.,
518 Prather, K., Hering, S., and Jimenez, J. L.: The influence of chemical composition
519 and mixing state of Los Angeles urban aerosol on CCN number and cloud
520 properties, *Atmos. Chem. Phys.*, 8, 5649–5667,
521 <https://doi.org/10.5194/acp-8-5649-2008>, 2008.
- 522 Deng, Z. Z., Ma, N., Liu, P. F., Xu,
523 W. Y., Zhao, C. S., Ran, L., Chen, J., Liang, Z., Liang, S., and Huang, M. Y.:
524 Size-resolved and bulk activation properties of aerosols in the North China Plain,
525 *Atmos. Chem. Phys.*, 11, 3835–3846, <https://doi.org/10.5194/acp-11-3835-2011>,
2011.
- 526 Dusek, U., Frank, G. P., Hildebrandt, L., Curtius, J., Schneider, J., Walter, S., Chand,
527 D., Drewnick, F., Hings, S., and Jung, D.: Size matters more than chemistry for
528 cloud-nucleating ability of aerosol particles, *Science*, 312, 1375–1378,
529 <https://doi.org/10.1126/science.1125261>, 2006.
- 530 Eichler, H., Cheng, Y. F., Birmili, W., Nowak, A., Wiedensohler, A., Brüggemann, E.,

531 Gnauk, T., Herrmann, H., Althausen, D., and Ansmann, A.: Hygroscopic properties
532 and extinction of aerosol particles at ambient relative humidity in South-Eastern
533 China, *Atmos Environ*, 42, 6321–6334,
534 <https://doi.org/10.1016/j.atmosenv.2008.05.007>, 2008.

535 Ervens, B., Cubison, M., Andrews, E., Feingold, G., Ogren, J. A., Jimenez, J. L.,
536 DeCarlo, P., and Nenes, A.: Prediction of cloud condensation nucleus number
537 concentration using measurements of aerosol size distributions and composition and
538 light scattering enhancement due to humidity, *J. Geophys. Res.-Atmos.*, 112,
539 <https://doi.org/10.1029/2006JD007426>, 2007.

540 Fu, G. Q., Xu, W. Y., Yang, R. F., Li, J. B., and Zhao, C. S.: The distribution and
541 trends of fog and haze in the North China Plain over the past 30 years, *Atmos.*
542 *Chem. Phys.*, 14, 11949–11958, <https://doi.org/10.5194/acp-14-11949-2014>, 2014.

543 Gomez-Hernandez, M., McKeown, M., Secrest, J., Marrero-Ortiz, W., Lavi, A.,
544 Rudich, Y., Collins, D. R., and Zhang, R.: Hygroscopic characteristics of
545 alkylammonium carboxylate aerosols, *Environ. Sci. Technol.*, 50, 2292–2300,
546 <https://dx.doi.org/10.1021/acs.est.5b04691>, 2016.

547 Guo, S., Hu, M., Lin, Y., Gomez-Hernandez, M., Zamora, M. L., Peng, J., Collins, D.
548 R., and Zhang, R.: OH-Initiated oxidation of m-xylene on black carbon aging,
549 *Environ. Sci. Technol.*, 50, 8605–8612, <https://dx.doi.org/10.1021/acs.est.6b01272>,
550 2016.

551 Gysel, M., Crosier, J., Topping, D. O., Whitehead, J. D., Bower, K. N., Cubison, M. J.,
552 Williams, P. I., Flynn, M. J., McFiggans, G. B., and Coe, H.: Closure study between
553 chemical composition and hygroscopic growth of aerosol particles during TORCH2,
554 *Atmos. Chem. Phys.*, 7, 6131–6144, <https://doi.org/10.5194/acp-7-6131-2007>,
555 2007.

556 Huang, R., Zhang, Y., Bozzetti, C., Ho, K., Cao, J., Han, Y., Daellenbach, K. R.,
557 Slowik, J. G., Platt, S. M., Canonaco, F., Zotter, P., Wolf, R., Pieber, S. M., Bruns,
558 E. A., Crippa, M., Ciarelli, G., Piazzalunga, A., Schwikowski, M., Abbaszade, G.,
559 Schnelle-Kreis, J., Zimmermann, R., An, Z., Szidat, S., Baltensperger, U., Haddad, I.
560 E., and Prévôt, A. S. H.: High secondary aerosol contribution to particulate
561 pollution during haze events in China, *Nature*, 514, 218–222,
562 <https://doi.org/10.1038/nature13774>, 2014.

563 IPCC: Climate change 2013: Scientific basis, Fifth assessment of the
564 Inter-governmental Panel on Climate Change, Cambridge University Press, 2013.

565 Jacobson, M. C., Hansson, H. C., Noone, K. J., and Charlson, R. J.: Organic
566 atmospheric aerosols: review and state of the science, *Rev. Geophys.*, 38, 267–294,
567 <https://doi.org/10.1029/1998RG000045>, 2000.

568 Jiang, R. X., Tan, H. B., Tang, L. L., Cai, M. F., Yin, Y., Li, F., Liu, L., Xu, H. B.,
569 Chan, P. W., Deng, X. J., and Wu, D.: Comparison of aerosol hygroscopicity and
570 mixing state between winter and summer seasons in Pearl River Delta region, China,
571 *Atmos. Res.*, 169, 160–170, <https://doi.org/10.1016/j.atmosres.2015.09.031>, 2016.

572 Jimenez, J. L., Canagaratna, M. R., Donahue, N. M., Prevot, A., Zhang, Q., Kroll, J.
573 H., DeCarlo, P. F., Allan, J. D., Coe, H., and Ng, N. L.: Evolution of organic
574 aerosols in the atmosphere, *Science*, 326, 1525–1529,

575 <https://doi.org/10.1126/science.1180353>, 2009.

576 Juranyi, Z., Gysel, M., Weingartner, E., DeCarlo, P. F., Kammermann, L., and
577 Baltensperger, U.: Measured and modelled cloud condensation nuclei number
578 concentration at the high alpine site Jungfraujoch, *Atmos. Chem. Phys.*, 10, 7891–
579 7906, <https://doi.org/10.5194/acp-10-7891-2010>, 2010.

580 Köhler, H.: The nucleus in and the growth of hygroscopic droplets, *T. Faraday Soc.*,
581 32, 1152–1161, <https://doi.org/10.1039/TF9363201152>, 1936.

582 Kulmala, M., Petäjä, T., Nieminen, T., Sipilä, M., Manninen, H. E., Lehtipalo, K., Dal
583 Maso, M., Aalto, P. P., Junninen, H., and Paasonen, P.: Measurement of the
584 nucleation of atmospheric aerosol particles, *Nat. Protoc.*, 7, 1651–1667,
585 <https://doi.org/10.1038/nprot.2012.091>, 2012.

586 Lance, S., Nenes, A., Medina, J., and Smith, J. N.: Mapping the operation of the DMT
587 continuous flow CCN counter, *Aerosol Sci. Tech.*, 40, 242–254,
588 <http://dx.doi.org/10.1080/02786820500543290>, 2006.

589 Lebo, Z. J., Shipway, B. J., Fan, J., Geresdi, I., Hill, A., Miltenberger, A., Morrison,
590 H., Rosenberg, P., Varble, A., and Xue, L.: Challenges for cloud modeling in the
591 context of aerosol-cloud-precipitation interactions, *B. Am. Meteorol. Soc.*,
592 <https://doi.org/10.1175/BAMS-D-16-0291.1>, 2017.

593 Li, Y., Zhang, F., Li, Z., Sun, L., Wang, Z., Li, P., Sun, Y., Ren, J., Wang, Y., Cribb,
594 M., and Yuan, C.: Influences of aerosol physiochemical properties and new particle
595 formation on CCN activity from observation at a suburban site of China, *Atmos.*
596 *Res.*, 188, 80–89, <https://doi.org/10.1016/j.atmosres.2017.01.009>, 2017.

597 Li, Z., Lau, W. K.-M., Ramanathan, V., Wu, G., Ding, Y., Manoj, M. G., Liu, J., Qian,
598 Y., Li, J., Zhou T., Fan, J., Rosenfeld, D., Ming, Y., Wang, Y., Huang, J., Wang, B.,
599 Xu, X., Lee, S.-S., Cribb, M., Zhang, F., Yang, X., Zhao, C., Takemura, T., Wang,
600 K., Xia, X., Yin, Y., Zhang, H., Guo, J., Zhai, P. M., Sugimoto, N., Babu, S. S., and
601 Brasseur, G. P.: Aerosol and monsoon climate interactions over Asia, *Rev.*
602 *Geophys.*, 54, 866–929, <https://doi.org/10.1002/2015RG000500>, 2016.

603 Li, Z., Daniel, R., and Fan, J. W.: Aerosols and their impact on radiation, clouds,
604 precipitation, and severe weather events, *Oxford Research Encyclopedias:*
605 *Environmental Science*, <https://doi.org/10.1093/acrefore/9780199389414.013.126>,
606 2017a.

607 Li, Z., Guo, J., Ding, a., Liao, h., Liu, J., Sun, Y., Wang, T., Xue, H., Zhang, H., and
608 Zhu, B.: Aerosols and boundary-layer interactions and impact on air quality, *Natl.*
609 *Sci. Rev.*, 4, 810–833, doi:10.1093/nsr/nwx117, 2017b.

610 Liu, P. F., Zhao, C. S., Bel, T. G., Hallbauer, E., Nowak, A., Ran, L., Xu, W. Y.,
611 Deng, Z. Z., Ma, N., Mildenberger, K., Henning, S., Stratmann, F., and
612 Wiedensohler, A.: Hygroscopic properties of aerosol particles at high relative
613 humidity and their diurnal variations in the North China Plain, *Atmos. Chem. Phys.*,
614 11, 3479–3494, <https://doi.org/10.5194/acp-11-3479-2011>, 2011.

615 Lopez-Yglesias, X. F., Yeung, M. C., Dey, S. E., Brechtel, F. J., and Chan, C. K.:
616 Performance evaluation of the Brechtel Mfg. Humidified Tandem Differential
617 Mobility Analyzer (BMI HTDMA) for studying hygroscopic properties of aerosol
618 particles, *Aerosol Sci. Tech.*, 48, 969–980,

619 <http://dx.doi.org/10.1080/02786826.2014.952366>, 2014.

620 Meng, J. W., Yeung, M. C., Li, Y. J., Lee, B. Y. L., and Chan, C. K.: Size-resolved
621 cloud condensation nuclei (CCN) activity and closure analysis at the HKUST
622 Supersite in Hong Kong, *Atmos. Chem. Phys.*, 14, 10267–10282,
623 <https://doi.org/10.5194/acp-14-10267-2014>, 2014.

624 Ng, N. L., Herndon, S. C., Trimborn, A., Canagaratna, M. R., Croteau, P. L., Onasch,
625 T. B., Sueper, D., Worsnop, D. R., Zhang, Q., and Sun, Y. L.: An Aerosol Chemical
626 Speciation Monitor (ACSM) for routine monitoring of the composition and mass
627 concentrations of ambient aerosol, *Aerosol Sci. Tech.*, 45, 780–794,
628 <http://dx.doi.org/10.1080/02786826.2011.560211>, 2011.

629 Petters, M. D., and Kreidenweis, S. M.: A single parameter representation of
630 hygroscopic growth and cloud condensation nucleus activity, *Atmos. Chem. Phys.*,
631 7, 1961–1971, <https://doi.org/10.5194/acp-7-1961-2007>, 2007.

632 Qiu, C., and Zhang, R.: Physiochemical properties of alkylammonium sulfates:
633 hygroscopicity, thermostability, and density, *Environ. Sci. Technol.*, 46, 4474–4480,
634 <https://dx.doi.org/10.1021/es3004377>, 2012.

635 Quan, J., Gao, Y., Zhang, Q., Tie, X., Cao, J., Han, S., Meng, J., Chen, P., and Zhao,
636 D.: Evolution of planetary boundary layer under different weather conditions, and
637 its impact on aerosol concentrations, *Particuology*, 11, 34–40,
638 <https://doi.org/10.1016/j.partic.2012.04.005>, 2013.

639 Ramanathan, V., Crutzen, P. J., Kiehl, J. T., and Rosenfeld, D.: Aerosols, climate, and
640 the hydrological cycle, *Science*, 294, 2119–2124,
641 <https://doi.org/10.1126/science.1064034>, 2001.

642 Rose, D., Gunthe, S. S., Mikhailov, E., Frank, G. P., Dusek, U., Andreae, M. O., and
643 Pöschl, U.: Calibration and measurement uncertainties of a continuous-flow cloud
644 condensation nuclei counter (DMT-CCNC): CCN activation of ammonium sulfate
645 and sodium chloride aerosol particles in theory and experiment, *Atmos. Chem.*
646 *Phys.*, 8, 1153–1179, <https://doi.org/10.5194/acp-8-1153-2008>, 2008.

647 Rosenfeld, D., U. Lohmann, G. B. Raga, C. D. O’Dowd, M. Kulmala, S. Fuzzi, A.
648 Reissell, and M. O. Andreae, Flood or drought: How do aerosols affect
649 precipitation?, *Science*, 321, doi:10.1126/science.1160606, 2008.

650 Schmale, J., Henning, S., Decesari, S., Henzing, B., Keskinen, H., Sellegri, K.,
651 Ovadnevaite, J., Pöhlker, M. L., Brito, J., Bougiatioti, A., Kristensson, A., Kalivitis,
652 N., Stavroulas, I., Carbone, S., Jefferson, A., Park, M., Schlag, P., Iwamoto, Y.,
653 Aalto, P., Äijälä, M., Bukowiecki, N., Ehn, M., Frank, G., Fröhlich, R., Frumau, A.,
654 Herrmann, E., Herrmann, H., Holzinger, R., Kos, G., Kulmala, M., Mihalopoulos,
655 N., Nenes, A., O’Dowd, C., Petäjä, T., Picard, D., Pöhlker, C., Pöschl, U., Poulain,
656 L., Prévôt, A. S. H., Swietlicki, E., Andreae, M. O., Artaxo, P., Wiedensohler, A.,
657 Ogren, J., Matsuki, A., Yum, S. S., Stratmann, F., Baltensperger, U., and Gysel, M.:
658 Long-term cloud condensation nuclei number concentration, particle number size
659 distribution and chemical composition measurements at regionally representative
660 observatories, *Atmos Chem Phys*, 18, 2853–2881,
661 <https://doi.org/10.5194/acp-18-2853-2018>, 2018.

662 Stokes, R. H., and Robinson, R. A.: Interactions in aqueous nonelectrolyte solutions. I.

663 Solute-solvent equilibria, *J. Phys. Chem.*, 70, 2126–2131,
664 <https://doi.org/10.1021/j100879a010>, 1966.

665 Stolzenburg, M. R., and McMurry, P. H.: Equations governing single and tandem
666 DMA configurations and a new lognormal approximation to the transfer function,
667 *Aerosol Sci. Tech.*, 42, 421–432, <http://dx.doi.org/10.1080/02786820802157823>,
668 2008.

669 Stolzenburg, M. R., and McMurry, P. H.: TDMAFIT user's manual, University of
670 Minnesota, Department of Mechanical Engineering, Particle Technology
671 Laboratory, Minneapolis, 1–61, 1988.

672 Sun, Y., Wang, Z., Dong, H., Yang, T., Li, J., Pan, X., Chen, P., and Jayne, J. T.:
673 Characterization of summer organic and inorganic aerosols in Beijing, China with
674 an Aerosol Chemical Speciation Monitor, *Atmos. Environ.*, 51, 250–259,
675 <https://doi.org/10.1016/j.atmosenv.2012.01.013>, 2012.

676 Swietlicki, E., Hansson, H. C., Hämeri, K., Svenningsson, B., Massling, A.,
677 McFiggans, G., McMurry, P. H., Petäjä, T., Tunved, P., Gysel, M., Topping, D.,
678 Weingartner, E., Baltensperger, U., Rissler, J., Wiedensohler, A., and Kulmala, M.:
679 Hygroscopic properties of submicrometer atmospheric aerosol particles measured
680 with H-TDMA instruments in various environments—a review, *Tellus B*, 60, 432–
681 469, <https://doi.org/10.1111/j.1600-0889.2008.00350.x>, 2008.

682 Tan, H., Xu, H., Wan, Q., Li, F., Deng, X., Chan, P. W., Xia, D., and Yin, Y.: Design
683 and application of an unattended multifunctional H-TDMA system, *J. Atmos.*
684 *Ocean. Tech.*, 30, 1136–1148, <https://doi.org/10.1175/JTECH-D-12-00129.1>, 2013.

685 Tritscher, T., Juranyi, Z., Martin, M., Chirico, R., Gysel, M., Heringa, M. F., DeCarlo,
686 P. F., Sierau, B., Prévôt, A. S. H., Weingartner, E., and Baltensperger, U.: Changes
687 of hygroscopicity and morphology during ageing of diesel soot, *Environ. Res. Lett.*,
688 6, <https://doi.org/10.1088/1748-9326/6/3/034026>, 2011.

689 Twomey, S.: Pollution and the planetary albedo, *Atmos. Environ.*, 8, 1251–1256,
690 [https://doi.org/10.1016/0004-6981\(74\)90004-3](https://doi.org/10.1016/0004-6981(74)90004-3), 1974.

691 Ulbrich, I. M., Canagaratna, M. R., Zhang, Q., Worsnop, D. R., and Jimenez, J. L.:
692 Interpretation of organic components from Positive Matrix Factorization of aerosol
693 mass spectrometric data, *Atmos. Chem. Phys.*, 9, 2891–2918,
694 <https://doi.org/10.5194/acp-9-2891-2009>, 2009.

695 Wang, L. T., Wei, Z., Yang, J., Zhang, Y., Zhang, F. F., Su, J., Meng, C. C., and
696 Zhang, Q.: The 2013 severe haze over the southern Hebei, China: model evaluation,
697 source apportionment, and policy implications, *Atmos. Chem. Phys. Disc.*, 13,
698 3151–3173, <https://doi.org/10.5194/acp-14-3151-2014>, 2014.

699 Wang, Y., Zhang, F., Li, Z., Tan, H., Xu, H., Ren, J., Zhao, J., Du, W., and Sun, Y.:
700 Enhanced hydrophobicity and volatility of submicron aerosols under severe
701 emission control conditions in Beijing, *Atmos. Chem. Phys.*, 17, 5239–5251,
702 <https://doi.org/10.5194/acp-17-5239-2017>, 2017.

703 Wang, Z., Wu, Z., Yue, D., Shang, D., Guo, S., Sun, J., Ding, A., Wang, L., Jiang, J.,
704 and Guo, H.: New particle formation in China: current knowledge and further
705 directions, *Sci. Total Environ.*, 577, 258–266,
706 <https://doi.org/10.1016/j.scitotenv.2016.10.177>, 2017.

707 Wu, Z. J., Zheng, J., Shang, D. J., Du, Z. F., Wu, Y. S., Zeng, L. M., Wiedensohler,
708 A., and Hu, M.: Particle hygroscopicity and its link to chemical composition in the
709 urban atmosphere of Beijing, China, during summertime, *Atmos. Chem. Phys.*, 16,
710 1123–1138, <https://doi.org/10.5194/acp-16-1123-2016>, 2016.

711 Ye, X., Tang, C., Yin, Z., Chen, J., Ma, Z., Kong, L., Yang, X., Gao, W., and Geng,
712 F.: Hygroscopic growth of urban aerosol particles during the 2009 Mirage-Shanghai
713 Campaign, *Atmos. Environ.*, 64, 263–269,
714 <https://doi.org/10.1016/j.atmosenv.2012.09.064>, 2013.

715 Zhang, F., Li, Y., Li, Z., Sun, L., Li, R., Zhao, C., Wang, P., Sun, Y., Liu, X., Li, J.,
716 Li, P., Ren, G., and Fan, T.: Aerosol hygroscopicity and cloud condensation nuclei
717 activity during the AC³Exp campaign: implications for cloud condensation nuclei
718 parameterization, *Atmos. Chem. Phys.*, 14, 13423–13437,
719 <https://doi.org/10.5194/acp-14-13423-2014>, 2014.

720 Zhang, F., Li, Z., Li, Y., Sun, Y., Wang, Z., Li, P., Sun, L., Wang, P., Cribb, M., Zhao,
721 C., Fan, T., Yang, X., and Wang, Q.: Impacts of organic aerosols and its oxidation
722 level on CCN activity from measurement at a suburban site in China, *Atmos. Chem.*
723 *Phys.*, 16, 5413–5425, <https://doi.org/10.5194/acp-16-5413-2016>, 2016.

724 Zhang, F., Wang, Y., Peng, J., Ren, J., Collins, D., Zhang, R., Sun, Y., Yang, X., and
725 Li, Z.: Uncertainty in predicting CCN activity of aged and primary aerosols, *J.*
726 *Geophys. Res.-Atmos.*, 122, <https://doi.org/10.1002/2017JD027058>, 2017.

727 Zhang, R., Khalizov, A. F., Pagels, J., Zhang, D., Xue, H., and McMurry, P. H.:
728 Variability in morphology, hygroscopicity, and optical properties of soot aerosols
729 during atmospheric processing, *P. Natl. Acad. Sci. USA*, 105, 10291–10296,
730 <https://doi.org/10.1073/pnas.0804860105>, 2008.

731 Zhang, S. L., Ma, N., Kecorius, S., Wang, P. C., Hu, M., Wang, Z. B., Größ, J., Wu, Z.
732 J., and Wiedensohler, A.: Mixing state of atmospheric particles over the North
733 China Plain, *Atmos. Environ.*, 125, Part A, 152–164,
734 <https://doi.org/10.1016/j.atmosenv.2015.10.053>, 2016. Zhang, Y., Du, W., Wang, Y.,
735 Wang, Q., Wang, H., Zheng, H., Zhang, F., Shi, H., Bian, Y., Han, Y., Fu, P.,
736 Canonaco, F., Prévôt, A. S. H., Zhu, T., Wang, P., Li, Z., and Sun, Y.: Aerosol
737 chemistry and particle growth events at an urban downwind site in the North China
738 Plain, *Atmos. Chem. Phys. Discuss.*, 2018, 1–29,
739 <https://doi.org/10.5194/acp-2017-889>, 2018.

740 Zhu, Y., Zhang, J., Wang, J., Chen, W., Han, Y., Ye, C., Li, Y., Liu, J., Zeng, L., Wu,
741 Y., Wang, X., Wang, W., Chen, J., and Zhu, T.: Distribution and sources of air
742 pollutants in the North China Plain based on on-road mobile measurements, *Atmos.*
743 *Chem. Phys.*, 16, 12551–12565, <https://doi.org/10.5194/acp-16-12551-2016>, 2016.

744
745
746
747
748

749 **Table 1.** Number fractions of different hygroscopic groups for different particle sizes.

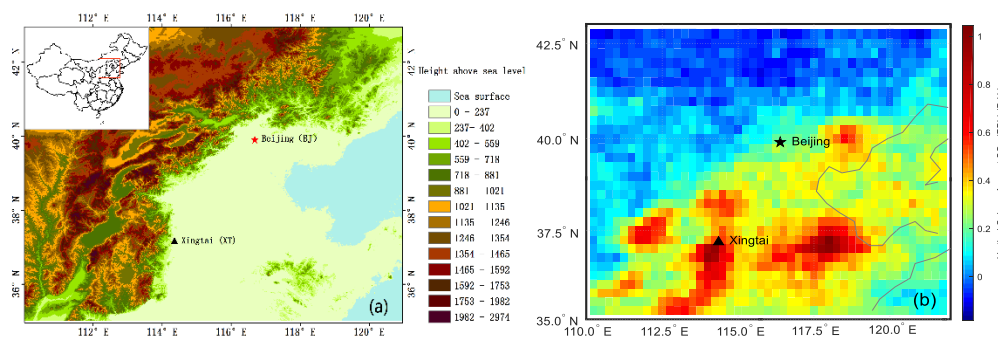
	40 nm	80 nm	110 nm	150 nm	200 nm
NH	5.1 %	5.0 %	5.1 %	5.0 %	5.7 %
LH	4.8 %	4.2 %	4.3 %	4.7 %	5.1 %
MH	90.1 %	90.8 %	90.6 %	90.3 %	89.2 %

750 NH: nearly hydrophobic; LH: less hygroscopic; MH: more hygroscopic

751

752

753

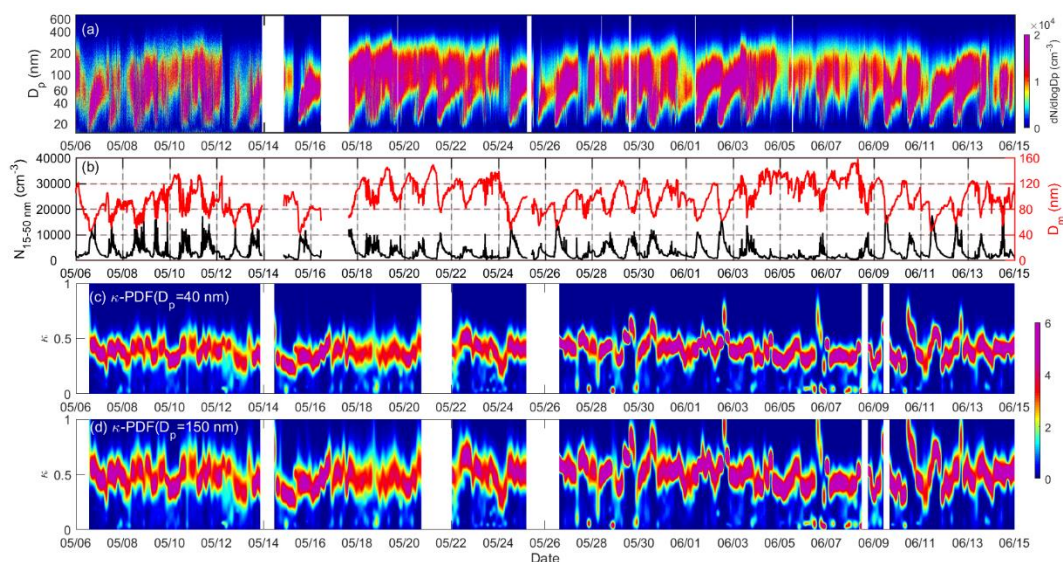


754

755 **Figure 1.** (a) Map showing the location of the sampling site and (b) the distribution of

756 mean SO_2 concentrations from May of 2012 to 2016.

757



758

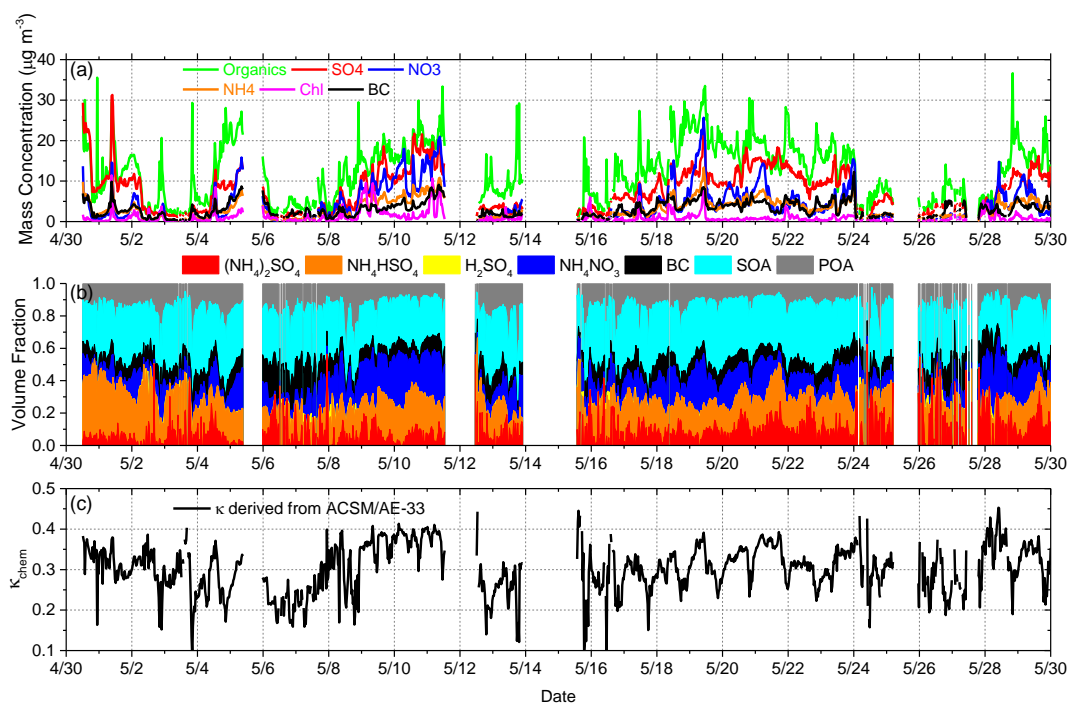
759 **Figure 2.** The time series of (a) the particle number size distribution, (b) the aerosol

760 number concentration in the 15–50 nm range ($N_{15-50 \text{ nm}}$) and the geometric mean

761 diameter (D_m), (c) the probability density function of κ_{gf} for 40-nm and (d) 150-nm

762 particles from 6 May to 15 June of 2016.

763
764



765

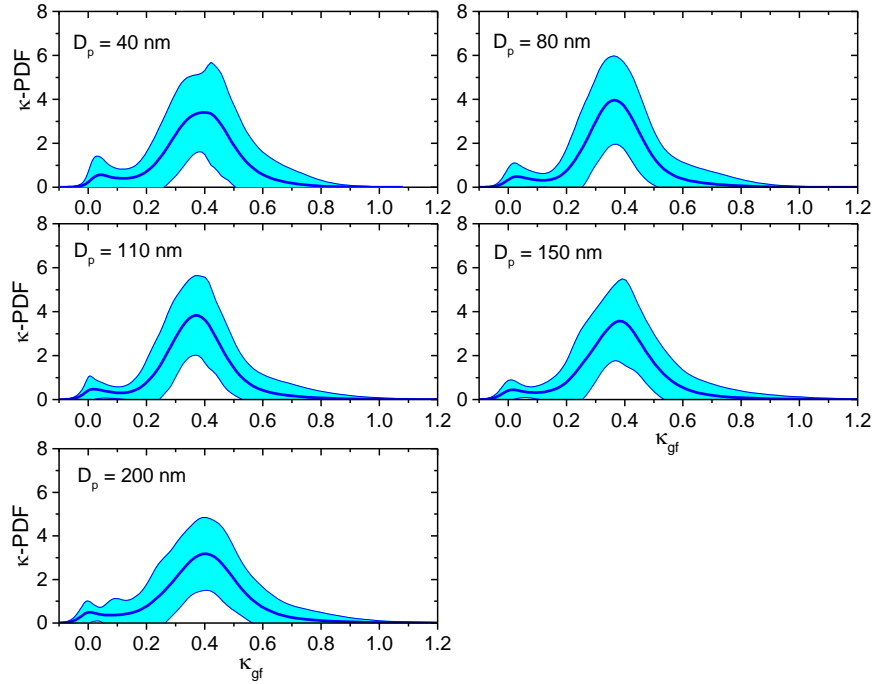
766 **Figure 3.** Time series of (a) the bulk mass concentration of aerosol species in PM_{10} , (b)

767 the volume fractions of POA, SOA, BC, and inorganics with the simplified

768 ion-pairing scheme, and (c) the hygroscopicity parameter derived from the chemical

769 composition (κ_{chem}).

770



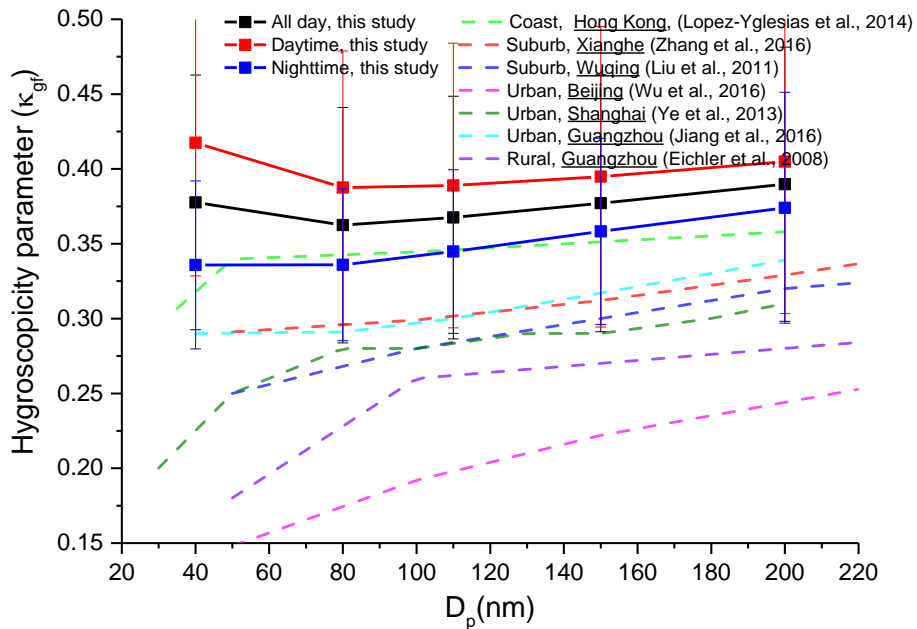
771

772 **Figure 4.** Mean probability density functions of κ_{gf} (κ -PDF) for different particle

773 sizes and their standard deviations (shaded areas) derived from H-TDMA data and

774 measured at RH = 85 %.

775

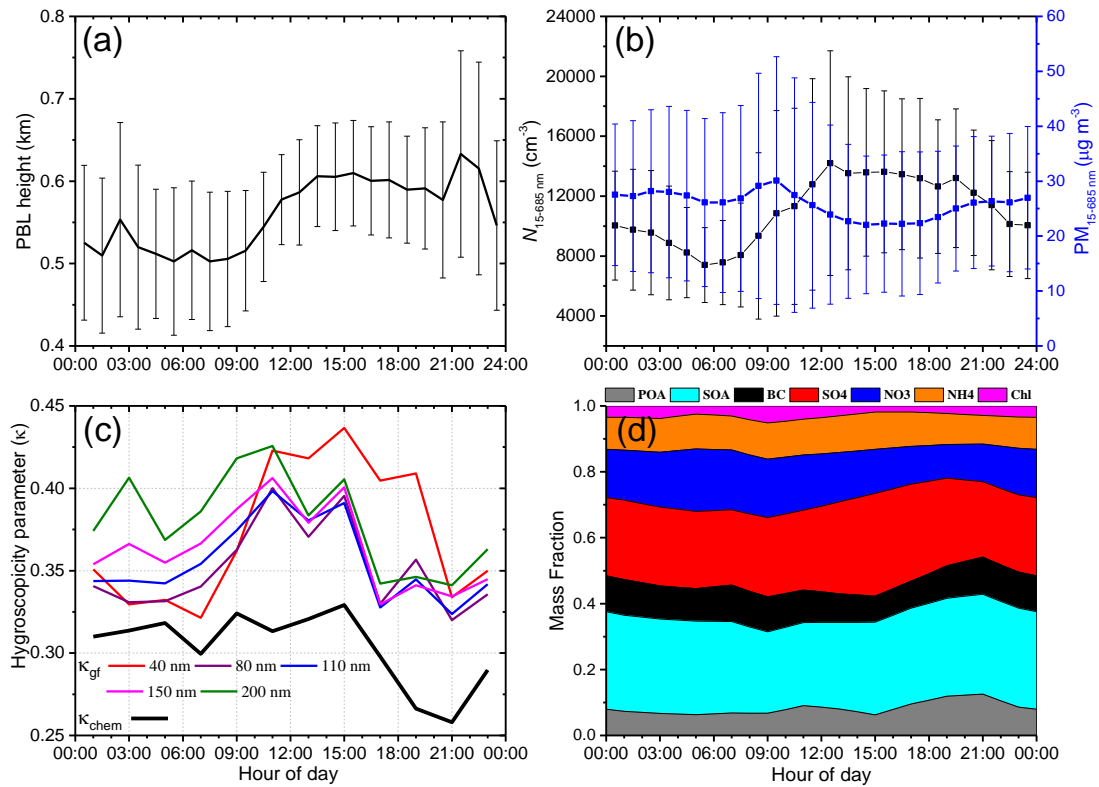


776

777 **Figure 5.** Size-resolved aerosol hygroscopicity parameter derived from H-TDMA

778 data at XT and at other sites in China.

779



780

781 **Figure 6.** Diurnal variations in (a) planetary boundary layer (PBL) height retrieved

782 from micropulse lidar data, (b) aerosol number and mass concentrations in the 15–685

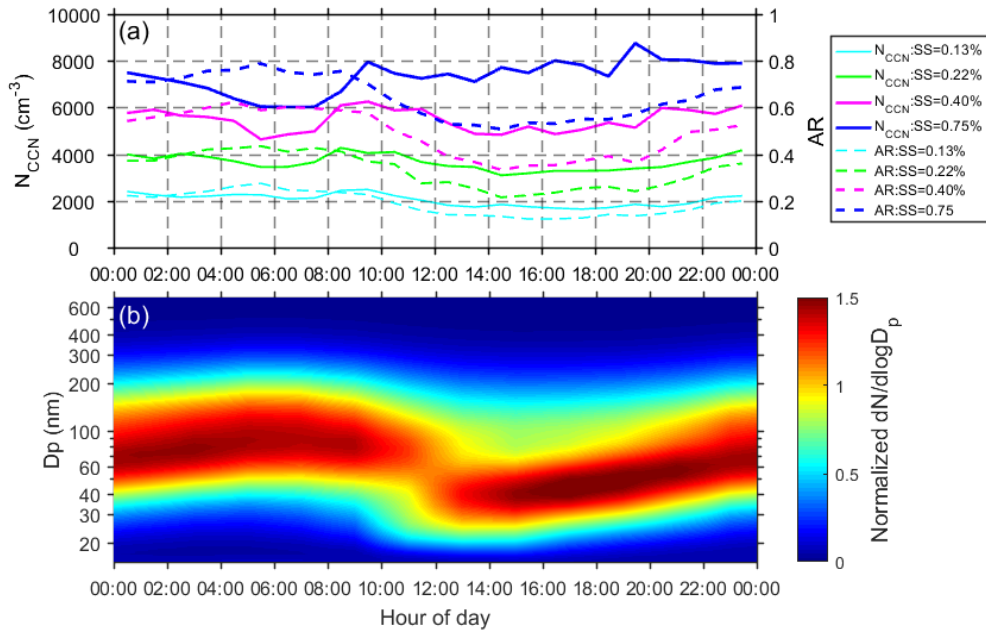
783 nm range ($N_{15-685 \text{ nm}}$ and $\text{PM}_{15-685 \text{ nm}}$, respectively) derived from the SMPS (an aerosol

784 density of 1.6 g cm^{-3} is assumed), (c) the hygroscopicity parameter derived from the

785 hygroscopic growth factor (κ_{gf}) and predicted from the bulk chemical composition

786 (κ_{chem}), and (d) the mass fractions of different species.

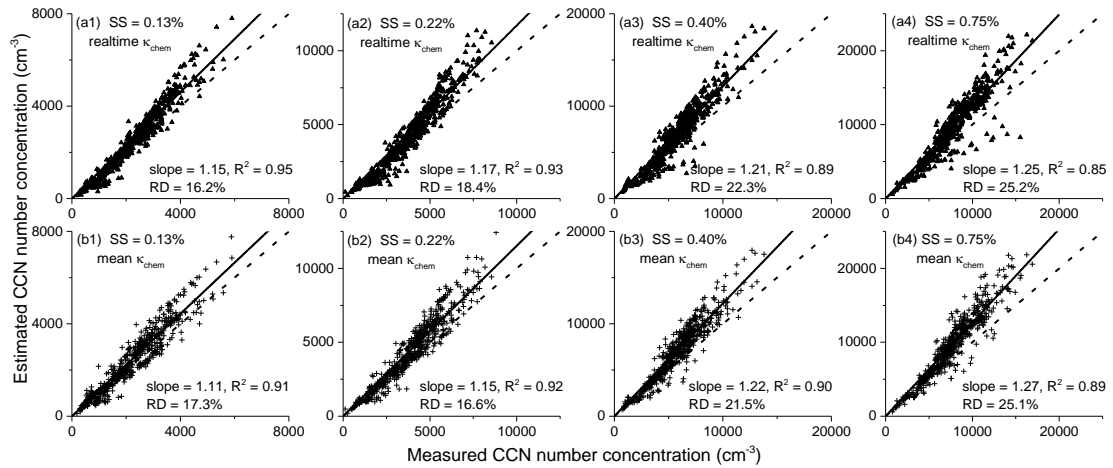
787



788

789 **Figure 7.** Diurnal variations in (a) CCN number concentration (N_{CCN}) and activation
 790 ratio (AR), and (b) the normalized aerosol size distribution in the 15–685-nm particle
 791 size range.

792

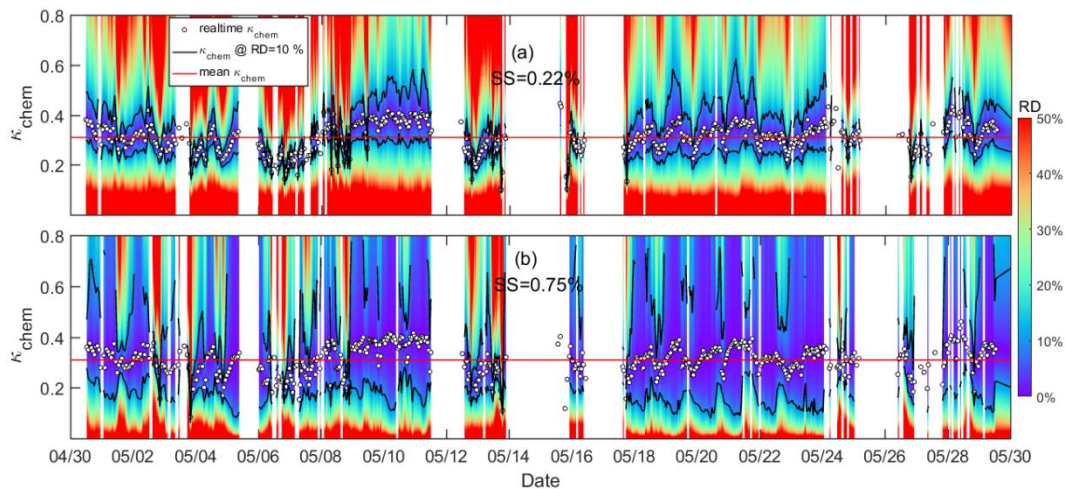


793

794

795 **Figure 8.** Estimated versus measured cloud condensation nuclei (CCN) number
 796 concentrations (N_{CCN}) for ambient aerosols at four different supersaturation (SS)
 797 levels. The N_{CCN} is estimated based on κ -Köhler theory using the real-time κ_{chem}
 798 (a1-a4) and the mean κ_{chem} (b1-b4). The slope and coefficient of determination (R^2)

799 of the linear regression and the relative deviation (RD) of estimated N_{CCN} (RD =
 800 $|N_{CCN_estimated} - N_{CCN_measured}| / N_{CCN_measured}$) are shown in each panel. The regression
 801 line is overlaid on the measurements (solid line) and the dashed line is the 1:1 line.
 802
 803



804
 805 **Figure 9.** Sensitivity of N_{CCN} estimates to κ_{chem} as a function of time at (a) $SS =$
 806 0.22% and (b) $SS = 0.75\%$. The color scale indicates the relative deviation (RD) of
 807 CCN estimates using the κ_{chem} value shown on the ordinate. In each panel, open
 808 circles show the real-time κ_{chem} . Note that RD is by definition zero at these points.
 809 The black line is κ at $RD = 10\%$ and the red line is the mean value for κ_{chem} (0.31).
 810 Figure S8 in the supplement shows the same plots but for $SS = 0.13\%$ and 0.40% .
 811